Cite this article
Santos DWM, Zornberg JG, Peitl Filho O and Portelinha FHM
Development of a transparent layered model for the study of pile-supported embankments on soft soils.
International Journal of Physical Modelling in Geotechnics,
https://doi.org/10.1680/jphmg.24.00066

Research Article
Paper 2400066
Received 25/10/2024; Accepted 29/07/2025

International Journal of Physical Modelling in Geotechnics

Development of a transparent layered model for the study of pile-supported embankments on soft soils

Dhionata Wyllian Moreira Santos
Civil Engineering Department, Federal University of Sao Carlos, Sao Paulo, Brazil

Jorge G. Zornberg
Department of Civil, Architectural and Environmental Engineering, The University of Texas at Austin, Austin, USA

Oscar Peitl Filho
Department of Materials Engineering, Federal University of Sao Carlos, Sao Paulo, Brazil

Fernando H. M. Portelinha
Civil Engineering Department, Federal University of Sao Carlos, Sao Paulo, Brazil (corresponding author: fportelinha@ufscar.br)

This study focuses on the construction process and challenges of a transparent, layered, two-dimensional physical model. The model was developed to enhance the comprehension of the mechanisms governing the behaviour of pile-supported embankments constructed over soft foundation soils. The methodology employed two types of 'transparent soil' techniques. Fused quartz particles, combined with a matching pore liquid, were utilised as the embankment base fill, while Laponite RD served as a surrogate for soft clay foundation conditions. The physical modelling techniques developed in this study were deemed suitable for advancing our understanding of internal deformations and the complexities of load transfer mechanisms in granular embankments over soft soils. These techniques not only provided observational results but also facilitated the quantification of shear, horizontal, and vertical strains. The findings of this study elucidate that the arching effect within the embankment's granular base fill resulted in the transfer of 80% of the applied stress to the piles. This arching efficiency remained consistent with increases in surcharge. The identified arching mechanism was related to the development of primary sub-vertical shear bands within the embankment base, complemented by a secondary triangular shear band.

Keywords: deformation/embankments/fused quartz/laponite/layered system/mechanisms/models (physical/model tests/soil arching/transparent soils

Notation

C_{LRD}	Laponite RD® content in %
C_{SPD}	content of sodium pyrophosphate decahydrate in %
m_{LRD}	mass of dry Laponite RD® in g
m_{SPD}	mass of sodium pyrophosphate decahydrate in g
m_w	mass of water added to the blend of Laponite RD® and sodium pyrophosphate decahydratein g

1. Introduction

Design methodologies for geotechnical systems commonly rely on the assessment of potential failure modes, which can be effectively investigated through physical model testing. In fact, physical modelling by way of visualisation of a soil mass's internal deformation has effectively contributed to an understanding of the mechanisms involved in numerous geotechnical problems, being particularly relevant for assessment of soil–structure interactions (Liu and Iskander, 2010). Often, observations conducted through the use of sensors installed within a soil mass are intrusive, leading to changes in the state of stresses of the medium under investigation. To overcome such problems, techniques have recently been developed that involve the use of transparent soils associated with visualisation and digital image processing techniques to investigate the behaviour of model-scale geotechnical systems (Ads *et al*., 2020a, 2020b; Cao, Liu, and Liu, 2011; Chen *et al*., 2019b, 2019a; Ezzein and Bathurst, 2014; Liu *et al*., 2020; Ma *et al*., 2022; Peng and Zornberg, 2019; Wang *et al*., 2022; Xu *et al*., 2021; Yang *et al*., 2022; Yuan *et al*., 2020; Zhang *et al*., 2020; Zhang *et al*., 2021).

Essentially, transparent soil techniques for granular materials involve the use of particles immersed in a pore fluid with a matching refractive index. Numerous attempts have been documented in the literature to implement such concept, including the use of glass beads, crushed glass, fused quartz particles, fused silica particles, clear plastic, and silica gel beads (Iskander *et al*., 2002a; Ganiyu *et al*., 2016; Ezzein and Bathurst, 2011; Liu and Iskander, 2010; Wei *et al*., 2019; Yang *et al*., 2020; Cao *et al*., 2011; Carvalho *et al*., 2015; Chen *et al*., 2021; Ezzein and Bathurst, 2014, 2011; Iskander *et al*., 2002b; Ma *et al*., 2022; Peng and Zornberg, 2019; Sadek *et al*., 2002a, 2002b; Zhang *et al*., 2021; Zhao and Ge, 2007). However, some of the aforementioned techniques present important disadvantages. For example, silica gel particles have been reported to plastically deform under low pressures, glass materials may undergo breakage, and plastic beads may be particularly expensive. Instead, the use of fused quartz particles was

found to be particularly suitable for physical modelling of a wide range of geotechnical systems using transparent granular soils. Ezzein and Bathurst (2014) characterised the shear strength properties of fused quartz particle materials based on direct shear and triaxial compression tests, showing that the material behaves similarly to quartz natural sand in terms of stress–strain and volumetric change behaviour.

In addition to transparent granular soils, efforts have also been reported to create transparent clay materials. Transparent clay surrogates have included amorphous silica powder (Gill and Lehane, 2001; Iskander *et al*., 2002a; Sadek *et al*., 2002, 2003; Liu *et al*., 2003; Iskander and Liu, 2010; Liu and Iskander, 2010; Ni, Hird, and Guymer, 2010; Guzman and Alfaro, 2016) and synthetic magnesium lithium phyllosilicate (Beemer *et al*., 2016; Beemer and Aubeny, 2012; Almikati *et al*., 2023; Ads *et al*., 2020a, 2020b; Pierozan *et al*., 2022; Wallace and Rutherford, 2015). Synthetic magnesium lithium phyllosilicate (Ads *et al*., 2020a), also known as laponite, has been reported to offer several advantages when used as transparent clay surrogate in geotechnical physical models, including adequate ranges of plasticity, rheology, and transparency (Ads *et al*., 2020a, 2020b; Iskander *et al*., 2002a; Kong *et al*., 2020; Liu *et al*., 2003; Ma *et al*., 2022; Wallace *et al*., 2018; Wallace and Rutherford, 2015; Pierozan *et al*., 2022; Almikati *et al*., 2023). Laponite is a synthetic smectite clay, comparable in structure to the natural clay mineral hectorite. Upon dispersion with distilled water, the synthetic clay hydrates, and swells, forming a transparent slurry that can then be consolidated under self-weight. The use of laponite in physical models requires that adequate visibility be achieved to depths relevant to the problems being analysed, thus ensuring testing accuracy, precision, and resolution. However, several inherent characteristics of laponite may affect its optical clarity and mechanical properties, including the laponite content, the type and dosage of additives, and the presence of inclusions that may develop within the laponite microstructure (Beemer *et al*., 2016). Wallace and Rutherford (2015) performed geotechnical laboratory tests, typically used to characterise soft clays, on laponite, including a series of laboratory vane tests, consolidation tests, and a series of permeability tests. The results demonstrated that laponite exhibits macroscopic geotechnical properties comparable to soft cohesive soils and can therefore be used as a soft clay surrogate in geotechnical physical model testing. More recently, Pierozan *et al*. (2022) investigated relevant factors affecting the optical and physical properties of laponite.

Use of the transparent soil technique to model homogeneous geotechnical problems, mostly involving soil–structure or soil–reinforcement interaction, has increased in recent years. However, while most geotechnical problems consist of multi-layered systems, physical modelling of geotechnical systems involving layers of multiple transparent materials has not been reported in technical literature. Embankments over soft soils represent a particularly relevant multi-layered geotechnical system, as it typically includes a granular layer acting as load transfer platform over which the embankment is seated. The system may also include deep foundations (e.g. concrete piles) supporting the embankment as well as geosynthetic reinforcements within the granular load transfer platform. The use of both concrete piles and geosynthetic reinforcements aims at enhancing the overall stability of the system or reducing settlements. The visualisation and quantification of deformations using a multi-layered pile-supported embankment for soft soil models can further an understanding of the mechanisms involved, including the development of soil arching mechanisms, development of horizontal stresses within the soft foundation soils, and the development of lateral restraint or membrane mechanisms when geosynthetic layers are utilised within the granular load transfer layer.

Several studies have been conducted to observe the arching effects by way of image analysis to capture internal deformations primarily using a trapdoor apparatus (Rui *et al*., 2016; Rui *et al*., 2019; Rui *et al*., 2020; Zhang *et al*., 2021). In the case of the authors, using active trapdoor mechanisms is efficient to evaluate arching mechanisms, but it does not reproduce the field reality in which incremental vertical pressures are applied. The authors believe that both stress conditions are not comparable given the significant differences of boundary conditions. However, additional evaluation is needed to understand the actual role of the soft foundation soil and piles in problems involving pile-supported embankments, which may be assessed through a multi-layered transparent model.

To gain a full understanding of the mechanisms involved in pile-supported embankments on soft soils and evaluate the potential of the transparent soil technique to simulate layered soil systems using transparent sands and clays, a transparent 1g physical model was developed in this study to investigate the mechanisms of stress transference involved in problems concerning pile-supported embankments over soft soil. This paper describes the experimental procedure developed to create a transparent layered soil system suitable to simulate pile-supported embankments over soft soils using fused quartz and laponite.

2. Transparent sand

2.1 Fused quartz particles

In this investigation, fused quartz particles were adopted as granular medium, which consist of a non-crystalline form of silicon dioxide (SiO_2) normally found in natural sands. Additional information on the manufacturing process and properties of fused quartz has been reported by Ezzein and Bathurst (2011) and Ferreira and Zornberg (2015). The fused quartz particles used herein had a purity of 99.995% and were obtained from the

grinding, sieving, and cleaning of crushed fused quartz tubes manufactured for the laboratory glassware industry. The grinding process was performed to produce a granular material with particle dimensions applicable in practice, scaled to prototype conditions, and limited to a maximum D_{50} of 1.75 mm, in accordance with the recommendation of Ezzein and Bathurst (2014) for achieving transparency up to a depth of 150 mm. The grinding process was carried out with a disk mill, which grinds the material by pressure and shearing action between two counteracting grinding disks with coarse interlocking teeth. The ground material automatically falls into a pre-set grinding gap in a collection drawer, and the ultimate grain size required can be defined by adjusting the gap width setting. The ground fused quartz material was then sieved to obtain particles with dimensions ranging from 1.19 to 2.38 mm. This particle size distribution was selected to provide adequate transparency with the matching liquid. The grinding process produced coarse sand material designated as angular according to ASTM D2488. Figure 1 shows the particle size distribution of the fused quartz as well as microscopy images of the particles retained by 2.83-, 2.38-, and 1.19-mm sieves. Coefficients of uniformity and curvature of 1.41 and 0.94, respectively, indicate a poorly graded sand according to ASTM D2487.

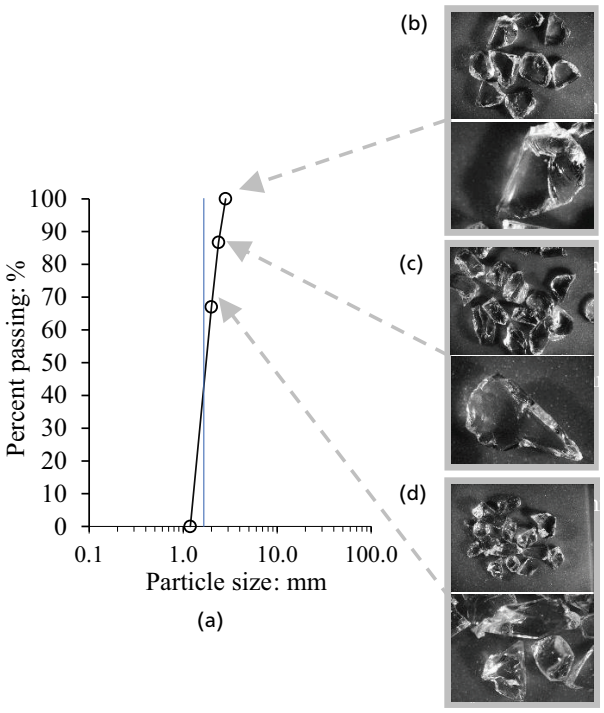

Figure 1. Grain size characteristics of fused quartz: (a) grain size distribution; (b) particles retained by 2.83-mm sieve; (c) particles retained by 2.38-mm sieve; and (d) particles retained by 1.19-mm sieve

2.2 Matching pore liquid

The approach used to prepare the liquid with matching refractive index involved mixing mineral oil (with a refractive index of 1.4779) and turpentine (with a refractive index of 1.4400), both of which are miscible and have higher and lower refractive indices, respectively, than the fused quartz particles. Different mixtures of turpentine and mineral oil were produced in a search of the refractive index of the fused quartz (1.4585). Results of refractive index of mixtures are presented in Figure 2. This test indicated that a 1:1 mass ratio of mineral oil and turpentine, at 22°C, led to the target refractive index. Because part of the saturation fluid is volatile, its refractive index stability was evaluated under constant temperature conditions, matching those of the experimental tests. The pore fluid was left in an open container and exposed to the atmosphere for 12 h, simulating the total exposure time during testing. Temperature is known to influence the optical properties of the fluid, particularly the refractive index; therefore, all procedures were conducted under controlled laboratory temperature to ensure consistency. The resultant transparent sand was achieved by filling the sand pores with the matching liquid as shown in Figure 3. The geogrid displayed in Figure 3 was used only for the illustration of the transparency of the fused quartz particles submersed in the matching pore liquid, and it is not applied in this investigation. The image in Figure 3(a) shows the geogrid embedded in the particles without the matching pore fluid. Figures 3(b) and 3(c) reveal the changes in transparency as transparent sand pores were with 60% and ≈100% of degree of saturation, respectively.

2.3 Geotechnical characterisation of transparent sand

A geotechnical characterisation of the transparent sand used in this investigation was carried out including grain size distribution, specific gravity, maximum and minimum void ratios, and shear

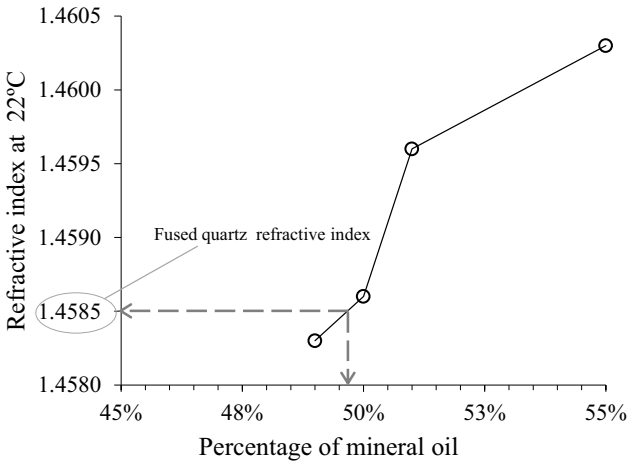

Figure 2. Refractive index of trial mixture plotted against percentage mineral oil added to turpentine

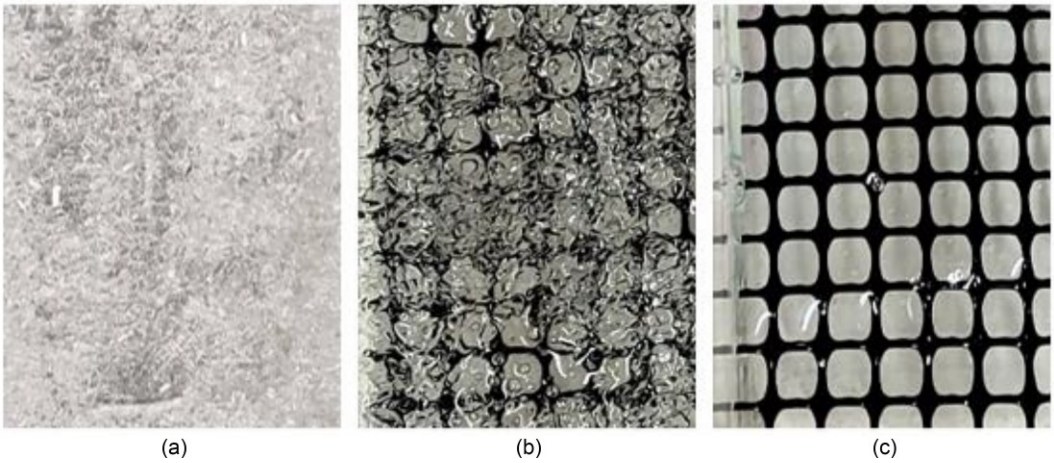

Figure 3. Pore saturation with matching pore liquid: (a) dry; (b) partially saturated; and (c) completely saturated transparent sand

strength of the crushed fused quartz by way of direct shear and triaxial tests. Results of the geotechnical characterisation are listed in Table 1.

The direct shear tests were performed under drained conditions in a shear box measuring 100 mm × 50 mm (diameter × height) at a constant displacement rate of 1 mm/min, following procedures established by ASTM D3080. Specimens were prepared initially dry at a relative density of 95%, which is the same as that adopted in the physical model. The pores of the specimen were subsequently filled with the matching pore liquid from the top to the bottom of the specimen. Tests were conducted under normal pressure of 25, 50, 75, and 100 kPa.

Figure 4 shows the direct shear test results for the pore liquid inundated fused quartz specimens. Results show a typical behaviour of dense granular materials with softening behaviour after a peak shear mobilisation (Figure 4(a)). As expected, specimens presented a reduction of volume at low shear displacements followed by an expansion (Figure 4(b)). At the critical state, it is observed an oscillation of shear stresses because of particles angularity and matching liquid lubrication. Stress oscillations at post-peak strength were also observed for saturated samples in Ezzein and Bathurst (2011) and Skinner (1969). This is attributed to particles angularity combined with the lubrication provided by the matching liquid. However, it must be clear that residual shear strength was not reached in the small-scale physical model evaluated in this investigation; therefore, it is deemed not to affect the overall behaviour. Peak friction angle of 49.3° was found from direct shear tests assuming a single linear envelope forced through origin. Results herein are consistent with those presented in the study by Ezzein and Bathurst (2011).

Triaxial compression tests under consolidated drained conditions were also conducted under confining pressures of 25, 50, 75, and 100 kPa. Tests were conducted in specimens saturated in the matching pore liquid. Procedures adopted for triaxial tests followed the recommendations of ASTM D7181 with displacement rate of 0.5 mm/min. Results of deviatoric stresses plotted against axial strain are depicted in Figure 5(a), while volumetric changes plotted against axial strains are plotted in Figure 5(b). Results show evidence of strain softening at post-peak shear strength, but less significant than that observed in direct shear tests and decreasing dilatancy with increasing confining pressure. The data

Table 1. Geotechnical properties of crushed fused quartz used in this study

Property	Notation	Test method	Value
Specific gravity	G_s	ASTM D854	2.220
Maximum dry unit weight	$\gamma_{dmáx}$: kN/m^3	ASTM D4253	13.00
Minimum void ratio	$e_{mín}$	—	0.71
Minimum dry unit weight	$\gamma_{dmín}$: kN/m^3	ASTM D4254	11.20
Maximum void ratio	e_{max}	—	0.99
Friction angle of liquid-saturated fused quartz from direct shear tests	$\phi_{Saturated}$: °	—	49.3°*
Friction angle of liquid-saturated fused quartz from triaxial tests	$\phi_{Saturated}$: °	ASTM D7181	48°*

* Assuming a single linear envelope forced through origin

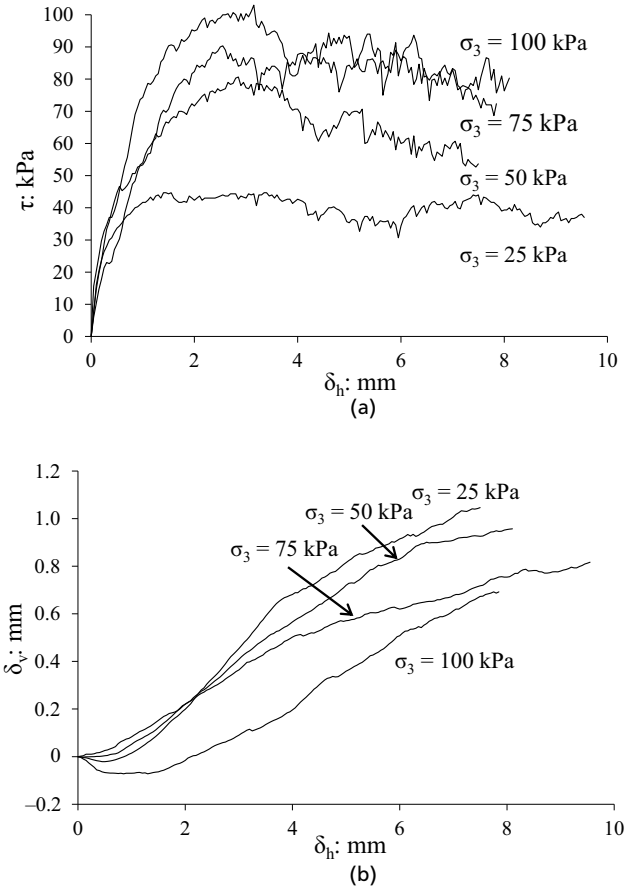

Figure 4. Direct shear test results: (a) shear stress plotted against horizontal displacements and (b) vertical displacements plotted against horizontal displacement

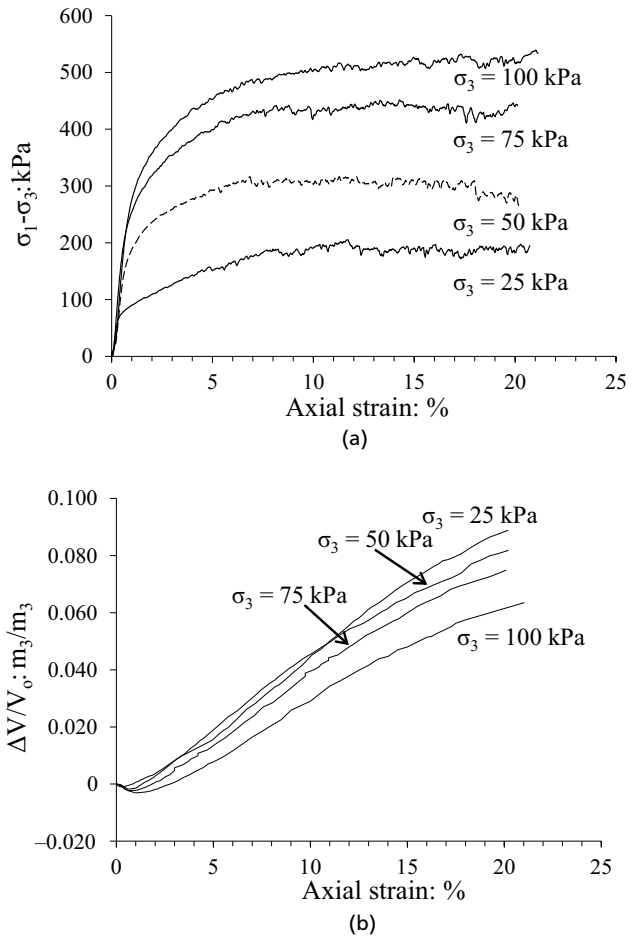

Figure 5. Triaxial test results of the granular material: (a) shear stress plotted against horizontal displacements and (b) vertical displacements plotted against horizontal displacement

sets for fused quartz material with the matching pore liquid are found to be typical for granular materials. The friction angle obtained from triaxial tests was 48° assuming a single linear enveloped forced through origin. Based on the test results provided herein, it can be observed that the fused quartz material behaves similarly to natural granular materials. Therefore, the use of this material in transparent models has the potential of reproducing mechanisms involved in most geotechnical problems.

3. Transparent soft clay

3.1 Laponite and additives

The clay surrogate for this study was made with Laponite RD manufactured by BYK Additives and Instruments. Laponite powder, chemically known as magnesium lithium phyllosilicate, is a synthetic layered silicate that becomes transparent when mixed with distilled water. Laponite is a 2:1 layered silicate, with structure similar to that of the natural clay mineral hectorite (Pierozan *et al*., 2022; Almikati *et al*., 2023). Some mineralogical and geotechnical characteristics of the same laponite used in this investigation can be found in Almikati *et al*. (2023). Optical and physical properties were reported by Pierozan *et al*. (2022). While laponite may be reasonably analogue to natural soft clays, there are limitations related to its long-term consolidation, very high void ratio (and thus low density), and high plasticity index values compared to natural soft clay materials (Beemer *et al*., 2016; Almikati *et al*., 2023). Mitigation of these problems was achieved by adding sodium pyrophosphate decahydrate (SPD) to facilitate preparation, achieve greater density, and increase the strength of the hydrated laponite as suggested in Almikati *et al*. (2023). Calculations of the percentages of SPD and laponite to be used in sample preparation were quantified as follows:

1. $$C_{\mathrm{LRD}}\,(\%) = \frac{m_{\mathrm{LRD}}}{m_{\mathrm{LRD}} + m_{\mathrm{w}} + m_{\mathrm{SPD}}}$$

$$2. \quad C_{SPD}\,(\%) = \frac{m_{SPD}}{m_{SPD} + m_w + m_{LRD}}$$

where C_{SPD} represents the dosage of SPD; C_{LRD} is the laponite powder content; m_{SPD} represents the dry mass of SPD; m_{LRD} represents the dry mass of laponite; and m_w represents the mass of distilled water. The amount of water added to prepare the mixtures and reach the total mass of water, m_w, was defined considering the initial moisture content in the SPD (67.92%) and laponite (7.84%).

Laponite mixtures were meticulously prepared at a room temperature of 21°C. The process involved gradually introducing air-dried powder into distilled water, with the powder composition precisely determined according to Equations 1 and 2, taking into account both laponite and SPD proportions. To ensure the optimal hydration of laponite and to achieve a uniform mixture, an overhead mixer with a rotation speed of 3000 rpm was employed. Each batch of laponite slurry was mixed for ≈15 min, yielding an average volume of 4.0 litres. Following the thorough mixing process, the hydrated laponite was carefully transferred to a testing box and allowed to rest for a seven-day duration at the same room temperature of 21°C. The testing box was sealed with plastic film to minimise any potential desiccation and evaporation before subsequent testing procedures.

3.2 Geotechnical characterisation of transparent clay

The geotechnical characterisation undertaken in this study included the determination of the liquid and plastic limits, as well as the undrained shear behaviour of the transparent clay. It should be noted that conducting consolidation tests on laponite proved impractical due to the excessively long time involved. Consequently, to simulate the mechanisms under examination, consolidation settlements were introduced, as we will discuss in the subsequent sections.

The liquid limit, plastic limit, and plasticity index were determined using the conventional method outlined in ASTM D4318. The tests were conducted with specific parameters, which were selected to ensure sufficient transparency in the physical model tests. The results of these tests revealed that the liquid limit, plastic limit, and plasticity index values for the transparent clay surrogate were 1325%, 1119%, and 206%, respectively.

Two distinct approaches were employed to characterise the undrained shear strength of the surrogate clay: ball penetration tests (BPT) and unconsolidated undrained triaxial tests. The BPT method, according to the protocols described in Ads *et al*. (2020b), involved penetration at rates of 4 mm/s, equivalent to ball diameter/s. Detailed information regarding the test setup and ball penetrometer dimensions can be found in Figure 6. In BPT, the bearing resistance (q) is defined as the force required to penetrate the ball into the transparent clay divided by the cross-sectional area of the ball.

For ball penetrometers, the ratio of undrained shear strength (S_u) to q, denoted as $N_b = q/S_u$, has been the subject of extensive research, with an average value of $N_b = 10.5$ for soft clay (Guzman *et al*., 2014). To minimise friction between the laponite and penetrometer shaft during penetration, the ball penetrometer was crafted from smooth stainless steel.

It is important to note that the primary objective of the BPT is to investigate potential chemical incompatibilities or physical interactions between the pore liquid and the hydrated laponite. While the BPT is not deemed precise for obtaining undrained shear strength, it proves practical for assessing chemical interactions between the materials. In contrast, unconsolidated undrained triaxial compression tests were considered a more reliable method for determining the undrained shear strength and stiffness of the transparent clay.

The BPT tests were performed in containers filled with saturated hydrated transparent clay. The transparent clay was exposed to the pore liquid of transparent sand for varying durations (7, 8, 9, and 10 days). The tests were conducted on transparent clay surrogates with two different compositions: C_{LRD} = 5% and C_{SPD}= 0.10%, and C_{LRD} = 7% and C_{SPD}= 0.14%. These tests were carried out after 0, 7, 24, 48, and 72 h of contact with the matching pore liquid.

Figure 7 presents the undrained shear strength (S_u) plotted against the depth of penetration during the BPT. The results represent an average of three measurements for each test condition. The

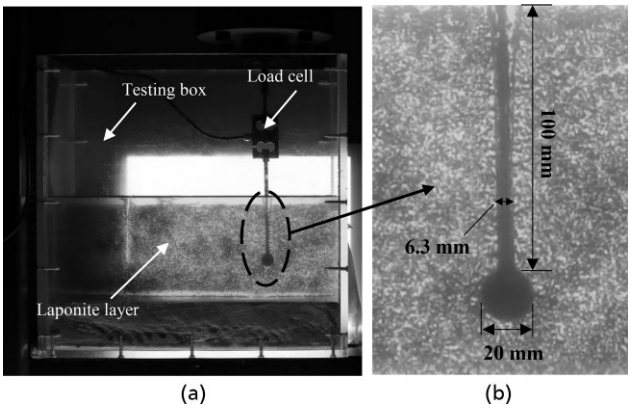

Figure 6. Ball penetration tests for characterisation of undrained shear strength: (a) test setup and (b) detail of ball penetrometer

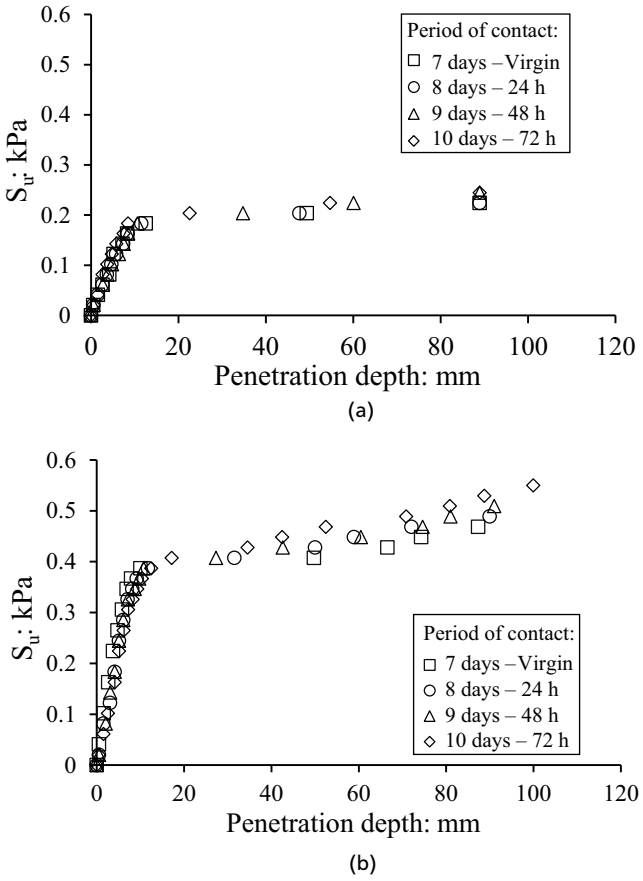

Figure 7. Undrained shear strength values obtained from ball penetration tests considering influence of contact period between hydrated laponite and transparent sand matching liquid: (a) C_{LRD} = 5%, C_{SPD} = 0.10% and (b) C_{LRD} = 7%, C_{SPD} = 0.14%

nominal undrained shear strength, as defined in Ads *et al.* (2020a), corresponds to two times the ball diameter, which is 40 mm.

The results reveal that the undrained shear strength (S_u) of the transparent clay surrogates varied within the range of 0.18–0.20 kPa when a combination of 5% laponite and 0.1% C_{SPD} was used. In contrast, when employing 7% laponite and 0.14% SPD, the S_u substantially increased to a range of 0.39–0.43 kPa. After a resting period of 72 h, contact between the laponite and the matching pore liquid resulted in a slight increase of 0.02 and 0.04 kPa, respectively. Consequently, it can be concluded that no significant chemical interaction occurred between the transparent clay surrogates and the matching pore liquid, which could have had a significant impact on the S_u. Nonetheless, it is important to note that appropriate precautions were taken to ensure consistent preparation times throughout the experimental programme for the physical model tests.

After observing no significant chemical incompatibility between the transparent clay and the matching pore liquid under the specified test conditions, unconsolidated undrained triaxial tests were conducted on specimens prepared with the same proportions as the model: 7% laponite and 0.14% SPD. These unconsolidated undrained triaxial tests followed the procedures outlined in ASTM D2850. The results, including deviatoric stresses and soil stiffness during the compression phase, are displayed in Figure 8. As expected in undrained conditions, the results demonstrate a consistent absence of changes in deviatoric stresses for the low confining pressures applied of 15 and 25 kPa. As higher confining pressure was applied, the laponite demonstrated a stress–strain behaviour typical of over consolidated clays. The undrained shear strength of the transparent clay was found to be around 0.4 kPa under confining pressures of 15 and 35 kPa, which increase to

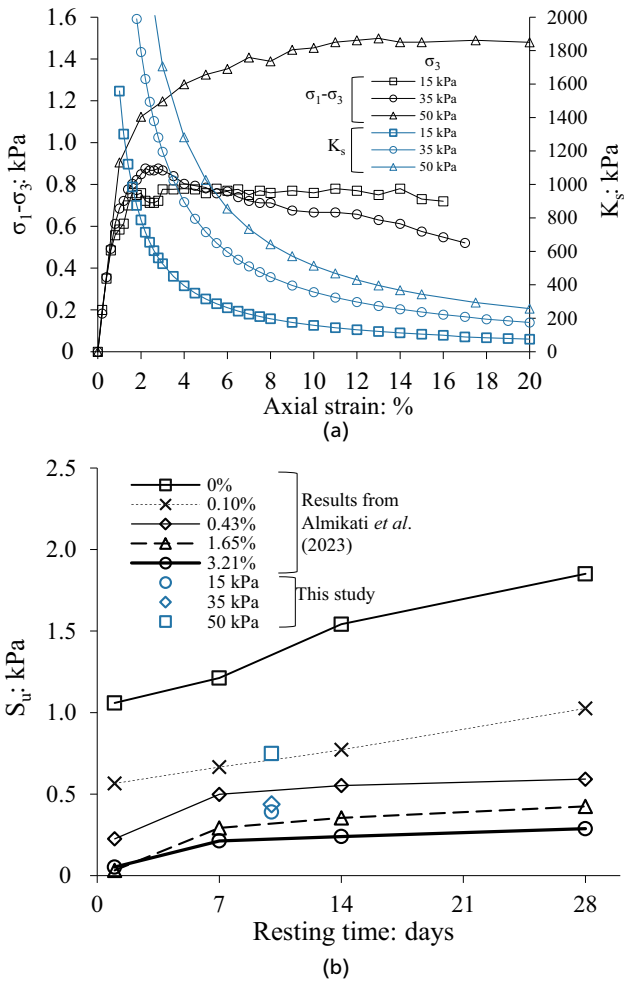

Figure 8. Shear strength characterisation of the laponite used as clay foundation: (a) undrained consolidated triaxial test results and (b) comparison of the laponite undrained shear strength to that obtained by Almikati *et al.* (2023)

around 0.7 at 50 kPa of confining pressure. It should be observed the similarity of undrained shear strength obtained using the BPT and triaxial tests. The tangent stiffness (K_s) at 5% of axial strain were measured as 350–1200 kPa depending on the level of confining pressure. This clay stiffness holds critical importance in evaluating stress distributions within the tested model, but at very low confining pressures (lower than 5 kPa). Figure 8(b) compares the undrained shear strength obtained from triaxial tests to results of mini-Vane tests conducted by Almikati *et al*. (2023) for a similar laponite adopted in this investigation. The comparison shows how consistent the results are obtained herein using triaxial test.

4. Model of transparent pile-supported embankment on soft soil

4.1 Testing setup

In this study, transparent two-dimensional (2D) reduced-scale physical models were meticulously produced to enable clear visualisation of the mechanisms involved in pile-supported embankments built on soft soils. The forthcoming sections of this paper report on the model's development and explore the results derived from the observation of displacements in tests conducted on the model.

The physical model was constructed on a 1:10 scale (model:prototype), and the testing configuration is illustrated in Figure 9. It comprised a 150-mm-thick transparent clay surrogate layer designed to replicate a soft soil foundation. Directly above, a 75-mm-thick layer of fused quartz, saturated with the matching pore liquid, emulated a granular load transfer layer typically found beneath an embankment. The simulated concrete piles, each featuring a square cross section measuring 20 mm and an overall length of 200 mm, were created using cement mortar. These piles were installed at a horizontal spacing of 200 mm (centre-to-centre). In addition, the pile system incorporated square pile caps with dimensions of 50 mm × 50 mm × 25 mm (L × W × H). To facilitate clear observation of the entire system, the physical model was enclosed within a rigid, transparent acrylic testing box.

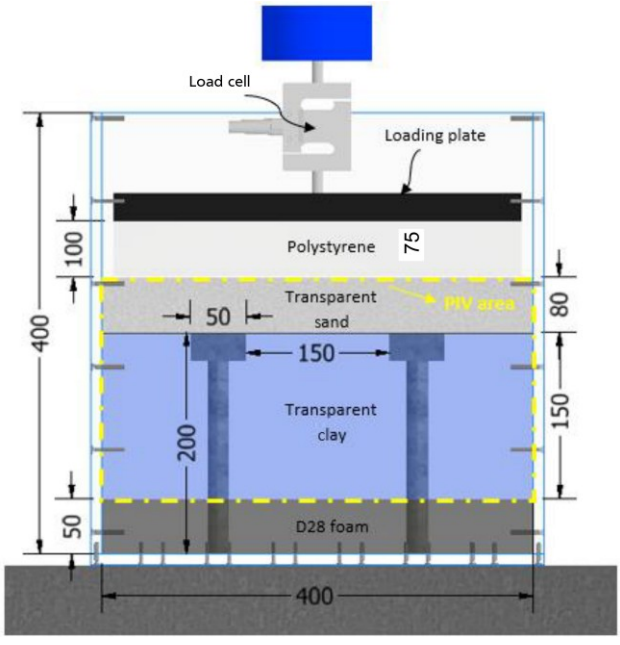

Figure 9. Configuration of the physical model

The transparent clay surrogate, characterised by a C_{LRD} of 7% and a C_{SPD} of 0.14%, was positioned within the testing box, where it rested for seven days before the initiation of testing. This material exhibited an undrained shear strength (S_u) of 1 kPa, which corresponds to 10 kPa at the prototype scale, agreeing with the typical undrained shear strength of soft clays in geotechnical practice.

Above the soft clay surrogate, a 75-mm-thick transparent sand layer was meticulously placed, attaining a relative density of 95%. Achieving the desired relative density involved employing a gentle compaction effort with a small hammer and compacting the material in layers of 5 mm. The mass of particles required for each compaction layer was accurately determined based on the maximum dry density and precisely compacted to fill the volume corresponding to each layer.

The dimensions of the various components in the physical model are detailed in Table 2 and were carefully selected to ensure similitude conditions between the model and prototype responses, following established guidelines (Iai, 1989; Viswanadham and König, 2004).

Due to the impractically lengthy time required for settlements to develop in the model, as a result of laponite consolidation, an engineered foam, commercially available as (D28), was introduced at the base of the model. This foam was employed to induce displacements and simulate compression-induced settlements in the reduced-scale model, mirroring the consolidation-induced settlements that occur in a prototype soft clay (see Figure 9). The compressibility characteristics of the foam were analysed to assist the interpretation of settlements in the physical model. Figure 10 displays the normalised settlements in relation to the applied

Table 2. Model physical parameters

Properties	Physical model
Thickness of transparent sand layer	75 mm
Thickness of transparent clay layer	150 mm
Square cap side length	50 mm
Square pile side length	20 mm
Horizontal spacing between piles	200 mm
Separation geotextile thickness	0.2 mm

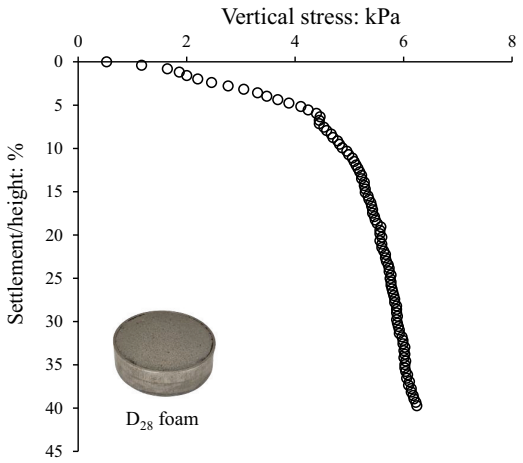

Figure 10. Compressive behaviour of D28 foam added to bottom of physical model

vertical stress for a foam sample with a diameter of 100 mm and a thickness of 25 mm. The results indicate that significant settlements are observed under applied vertical stresses exceeding 5 kPa.

To replicate the stress transfer characteristics of an embankment resting over a granular intermediary layer, a 100-mm layer of expanded polystyrene foam was placed between the top of the transparent granular layer. This foam layer acted as a compressible intermediary between the rigid load plate and the physical model. Subsequently, loading tests were conducted on the pile-supported embankment physical model using a universal testing machine, with a displacement rate of 2 mm/min. The testing was discontinued once an axial load corresponding to 30 kPa of vertical stress was achieved, as this value corresponds to the stress limit of the testing box.

4.2 Preparation of the layered system and plane of analysis

Defining a clear and consistent plane of analysis is essential when applying digital image correlation (DIC). For this reason, we adopted a specific central plane, located within the interior of the model, to minimise boundary effects and provide a representative view of the soil mass movement. This plane was defined by seeding particles, which required us to conduct the experiment in two construction phases.

The model construction began with the placement of engineered foam at the bottom of the container. The setup was then positioned on a bench to install a temporary acrylic plate, which facilitated the formation of an opaque plane of marker particles within the transparent clay layer. Laponite was subsequently poured into the testing box while the container remained in a horizontal position. After forming a 100-mm-thick (central plane) laponite layer, the filling process was paused, the container sealed, and the material left to cure for 24 h. The opaque plane of marker particles was then prepared, and the remaining volume was filled as the container was gradually restored to its original position. Following resealing, the transparent clay was allowed to consolidate under its own weight for 7 days, consistent with the procedure described by Wallace and Rutherford (2015), who reported minimal strength gains beyond this period. Following the laponite curing period, concrete piles were installed, after which a woven geotextile was placed over the laponite layer to prevent any mixing with the transparent sand. The transparent sand layer was subsequently prepared. This nonwoven geotextile is flexible enough and not continuous (cut) to avoid contributing to any reinforcement, serving only as a separator. The granular material was compacted outside the testing box using a specifically developed apparatus. Once compacted, liquid was introduced from the bottom up to minimise the formation of air bubbles. Any remaining bubbles were carefully removed using a needle, and the process was repeated until the desired height was reached.

The apparatus (380 mm × 50 mm × 16 mm; length × width × height) was specifically developed to precisely create the opaque plane of marker particles within the transparent sand, aligning with the analysis plane within the laponite layer. The device's movable components formed a rectangular prism, and the central 5-cm strip of each layer was fabricated outside the main container. After being filled with quartz, the device was locked, rotated, and placed on the piles to position the plane vertically. All faces, except the movable base, were surrounded by quartz to confine the assembly. The base was then removed, and the respective layer was then saturated from bottom to top, any air bubbles were removed using a needle, and this process was repeated until the desired total height was reached.

4.3 Quantification of deformations in the transparent physical model

Processing of images collected during testing facilitated determination of the displacement field within the soil mass at different times during loading. A camera connected to an image tethering software programme was used to capture the transparent side of the box. Blackouts were used behind the camera to reduce reflections on the transparent frontal wall of the box and lighting equipment was placed on either side of the front wall to enhance the light intensity and uniformity. DIC techniques were used to analyse the digital images collected during testing. Ncorr, an open-source MATLAB-based DIC software, was used in this investigation (Blaber *et al.*, 2015). DIC involves cross-correlation between successive images in an image stack. Cross-correlation techniques are used to identify the best match among targets (sub-image or group of pixels) in consecutive images by

comparing each image to the preceding one. Matching also enables motion detection (movement, deformation, velocity, and acceleration profiles). Details on this technique are found in Morsy *et al*. (2019) and Ezzein and Bathurst (2014). Black seeding particles were added to the transparent sand to provide additional colour contrast with the sand and thus improve images for DIC. Figure 11 shows an image of the physical model prepared for testing. Images were captured during testing using a Canon T6i digital camera with a resolution of 24.2 megapixels operating at a frequency of one picture per second. The effectiveness of DIC technology relies on the ability of the opaque layer to produce a high-quality stochastic pattern. To achieve this, the coverage rate of marker particles was carefully calibrated by selecting an appropriate quantity for the target plane, ensuring maximum accuracy. This precision is evident in the DIC images presented in the study, which exhibit no loss of accuracy and fully cover 100% of the analysed plane.

5. Results and discussions

5.1 Vertical displacements

The observation of the distribution of vertical displacements across the model section during testing plays a fundamental role in enhancing our understanding of the arching effect within the granular load transfer layer beneath the embankment. Furthermore, it offers valuable insights into the mechanical response of the soft foundation soil.

The displacement profiles, obtained by quantifying the vertical movements of the seeding particles embedded in both the transparent granular layer and the underlying transparent soft clay, are depicted in Figure 12. Within the plots, the black and blue profiles correspond to the displacements within the granular and clay layers, respectively. The red line denotes the vertical displacement at the level of the separation geotextile layer. The co-ordinate origin corresponds to the lower left corner of the physical model.

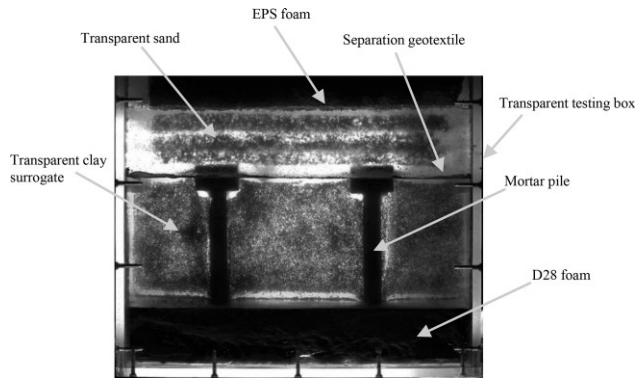

Figure 11. Image of transparent layered system adopted as a model of a pile-supported embankment over soft soil

The various loading stages presented in Figure 12 correspond to vertical applied pressures of 15, 20, 25, and 30 kPa. These profiles illustrate the development of a yielding zone between the pile caps and the stationary passive soil mass above the caps. Furthermore, they show an increase in yielding mass displacements increasing applied load, with this effect extending into the soft foundation soil at reduced rates. It is important to note that as the applied surcharge increases, vertical displacements at the base of the granular layer increase more at the centre of the distance between piles compared to those at the periphery of the caps. This relative settlement leads to the development of a shear band.

To facilitate the comparison of vertical displacement profiles under increasing load levels (15, 20, 25, and 30 kPa), two reference sections were defined for each stage, as shown in Figure 12. Sections without primes (e.g. A–A) intersect the midpoint between adjacent piles, while primed sections (e.g. A′–A′) pass through the centre of the piles. The vertical displacement profiles along all selected sections, after each surcharge stage employed in the test, are presented in Figure 13. The black curves represent the profiles from the mid-region between the piles, whereas the red curves correspond to the area over the caps. In sections, overall increases in vertical displacements were observed as the applied surcharges increased. Generally, the greatest displacements occurred at the upper part of the granular layer, with reducing displacements towards the base.

Vertical displacements exhibited a lower magnitude along the primed reference sections (e.g. A′–A′) positioned over the pile caps, when compared to the corresponding unprimed sections crossing the midpoint between adjacent piles. This behaviour characterises the regions above the caps as a relatively stationary passive granular mass. A notable observation was the nearly linear reduction in vertical displacements with increasing depth, spanning from the top of the granular layer to the base of the soft foundation soil. It might have been expected that the presence of the highly compressive clay layer (and foam layer) in relation to the granular layer would result in greater vertical displacements. However, the load transfer granular layer proved effective in mitigating these vertical displacements. This reduction in vertical displacements with depth within the clay layer also suggests that the granular layer contributes to reducing stresses overlying the clay layer. In addition, there was a slight reduction in vertical displacements at the separation geotextile layer, which might be attributed to a minimal stress mobilisation, as precautions taken to ensure that this material was not anchored directly over the pile caps.

Figure 14 illustrates the relationship between the applied vertical stress and the settlements at the bottom surface of the granular load transfer layer. The shape of the curve indicates that the pile-supported embankment model did not experience an overall failure. As stress was applied, the transparent sand mass between the piles (referred to as the yielding sand mass) exhibited more

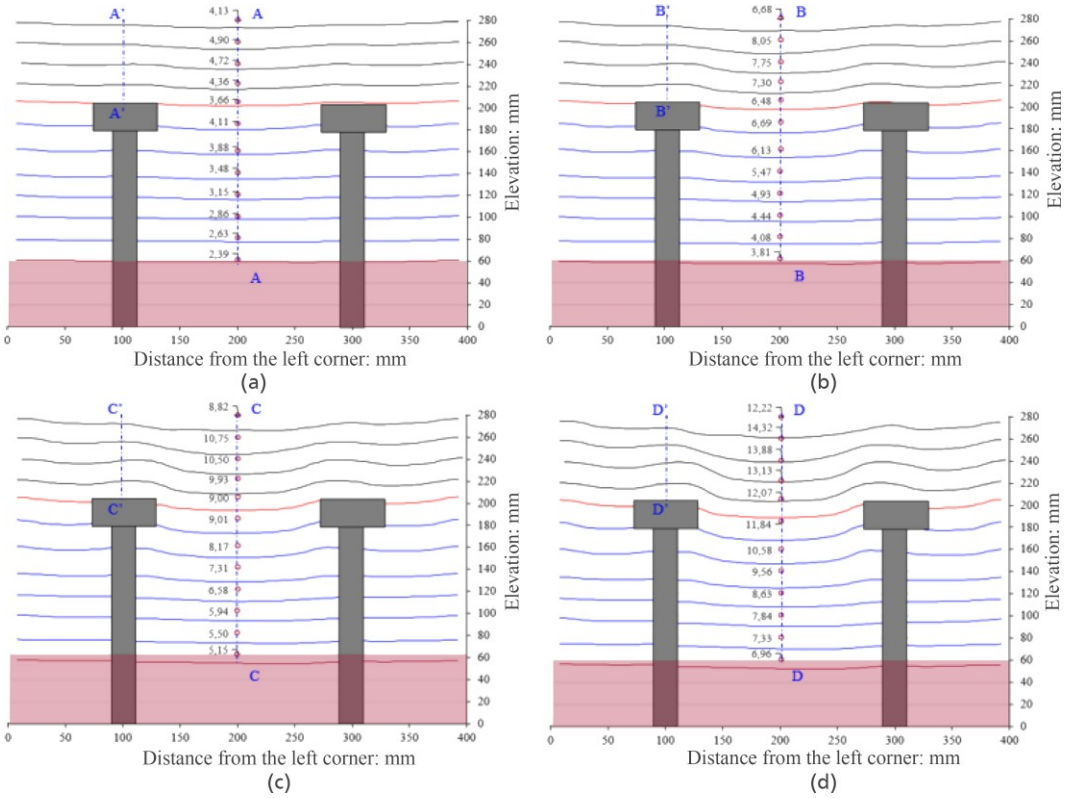

Figure 12. Distribution of vertical displacements at applied loads of (a) 15 kPa; (b) 20 kPa; (c) 25 kPa; and (d) 30 kPa

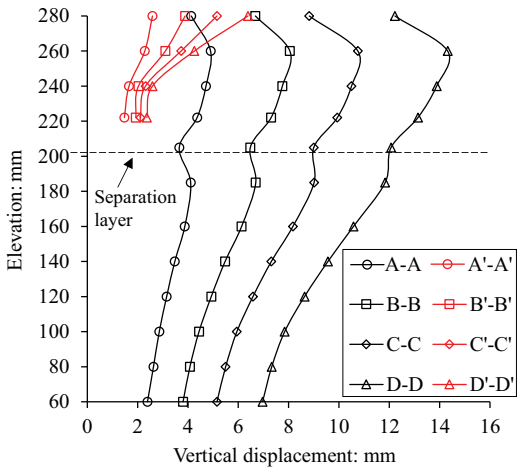

Figure 13. Distribution of vertical displacements at applied loads of (a) 15 kPa; (b) 20 kPa; (c) 25 kPa; and (d) 30 kPa

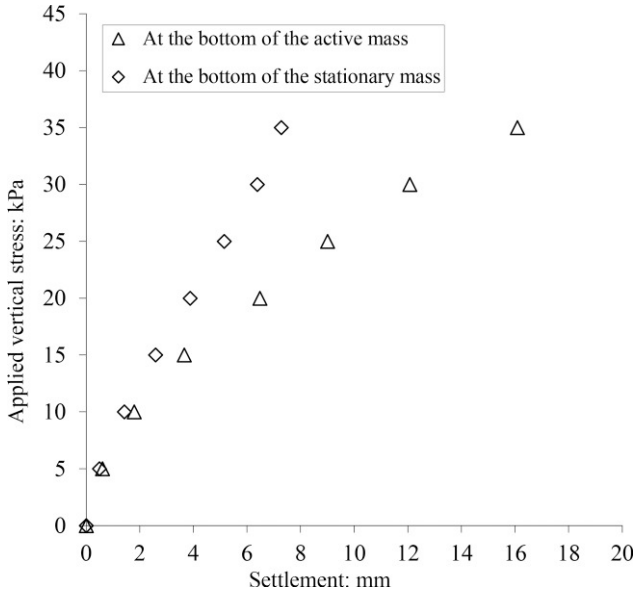

Figure 14. Applied vertical stress at load plate plotted against settlements measured at bottom of yielding and stationary masses

significant settlements. This relative displacement between the yielding and stationary masses is a critical factor in activating soil arching and reducing the stresses transmitted through the soft soil.

Consequently, this leads to an increase in stress over the pile caps and piles. Notably, significant relative displacements only manifested for vertical stresses exceeding 10 kPa.

5.2 Horizontal displacements

Analysing the distribution of horizontal displacements between piles can provide insights into arching mechanisms and allow for qualitative observations of the development of horizontal stresses along the pile shafts. Figure 15 shows the distribution of horizontal displacements in the physical model subjected to applied surcharges of 15, 20, 25, and 30 kPa. Vertical red lines marked at various distances from the left corner of the model serve as reference lines, indicating zero displacements. These lines help emphasise the magnitude of horizontal displacements resulting from the applied surcharges on the model's top surface. Notably, within the yielding mass, the portion of soil near the mid-height at the centre of the sand layer (ranging from 200 to 270 mm from the left corner) moves outward from the pile caps. This outward movement implies a lateral distribution of stresses and compression, supporting the principles described by Terzaghi (1943). However, the test shows that the lateral compression does not occur precisely at the centre of the active soil mass, indicating a slight eccentricity in stress distribution.

It should be also noted that lateral earth pressures also develop from the stationary mass towards the active mass located between the piles, resulting from the vertical compression over the caps and the expansion of the dense granular material, as similarly reported by Rui *et al*. (2020). These mechanisms enhance the mobilisation of friction between the stationary and active soil masses and are crucial for the development of soil arching. In addition, the soil particles at the base of the granular layer were observed to move towards the piles, indicating a flexural behaviour.

At lower vertical stress levels, higher values of horizontal displacement tend to be concentrated at the centre of the physical model (Figures 15(a) and 15(b)). However, with an increase in surcharge, greater displacements began to manifest also near and at the shaft of the piles. The maximum horizontal displacement recorded at the centre of the granular layer is highlighted in blue in Figure 15. It is worth noting that the maximum displacement, when considered along the height of the granular layer within the active mass, diminishes to near zero at an elevation of ≈220 mm. This can be interpreted as the depth of the neutral axis, or the inflection point for that specific displacement profile. Significant horizontal displacements were observed at a quarter of the distance from the top of the pile, indicating the development of

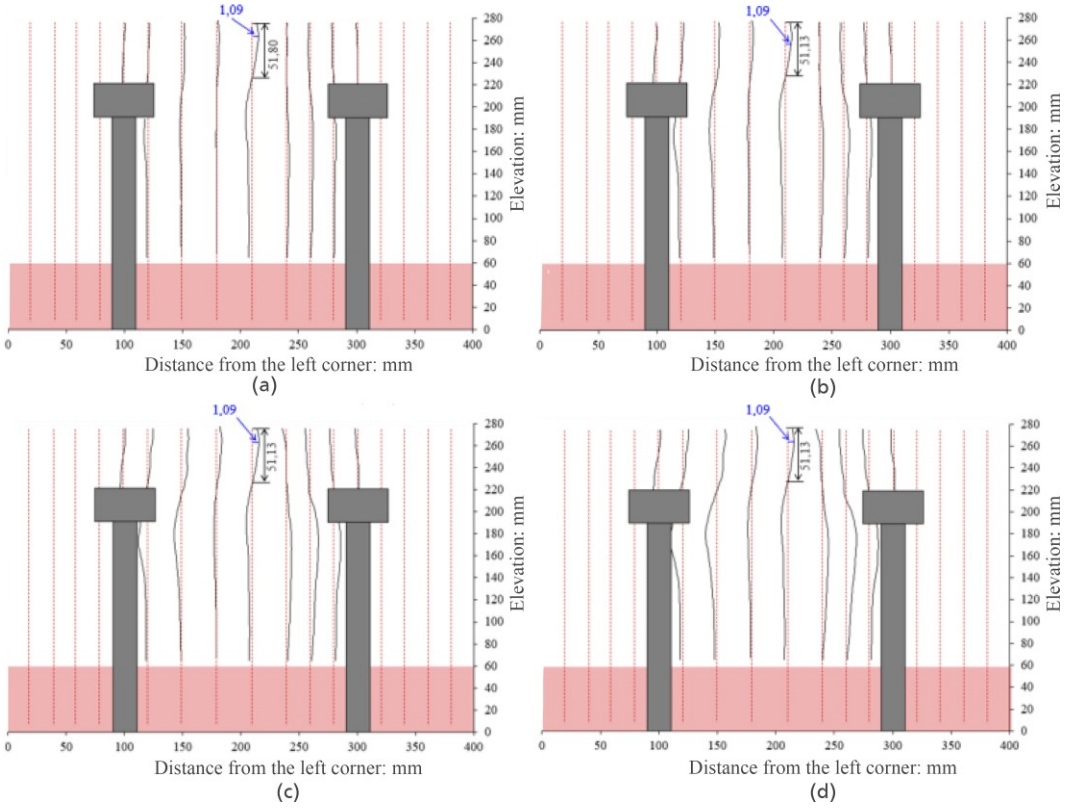

Figure 15. Distribution of horizontal displacements for applied loads of (a) 15 kPa; (b) 20 kPa; (c) 25 kPa; and (d) 30 kPa

horizontal stresses within the clay layer. Consequently, this development resulted in the lateral deflection of the piles, as depicted in Figure 16.

5.3 Load transfer mechanisms

To offer a comprehensive insight into the mechanisms at play within the physical model, the distribution of shear, vertical, and horizontal strains is provided in Figures 17–19, respectively.

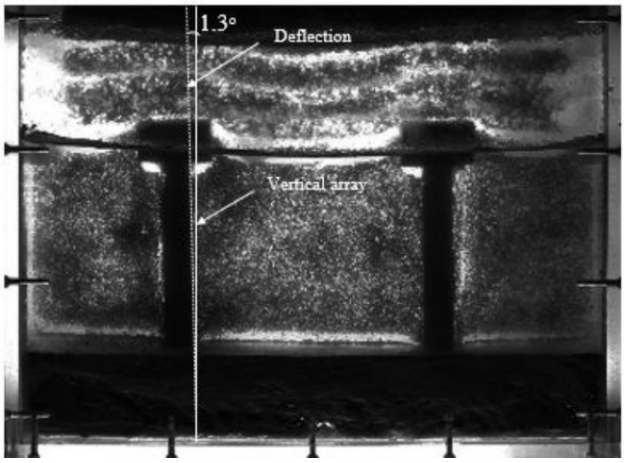

Figure 16. Image of pile deflection

These figures depict the strain distributions for applied surcharges of 15, 20, 25, and 30 kPa.

The shear band results illustrated in Figure 17 suggest a triangular expansion pattern outlined by the red dashed lines. However, a trapezoidal to square pattern of shear band is observed potentially because of the relatively large spacing between piles. Notably, neither the primary shear band (indicated by black dashed lines) with its trapezoidal (or sub-horizontal) shape nor the secondary triangular shear band exhibited significant alterations in shapes with increasing applied loads. In this stage, there was a greater inclination of the primary shear band surface and a reduced inclination of the secondary triangular pattern. This observation contrasts with the rectangular shear deformation pattern reported by Rui *et al*. (2016) under similar conditions. It is important to note that the conclusions drawn by the aforementioned authors were based on multi-trapdoor tests, which imposed different stress conditions compared with the incremental vertical external loads employed in our study. Furthermore, it is worth noting that there appears to be a trend of a rectangular deformation pattern for the pile located on the left side, whereas an inclined pattern is observed for the pile on the right. This distinction may result from some small eccentricity generated during the tests. While the shear band that developed within the granular layer extended into the clay layer, the direction of shear mobilisation was observed to shift within the soft soil to a rectangular pattern. The mobilisation of shear within the clay soil occurred primarily along the contact area with

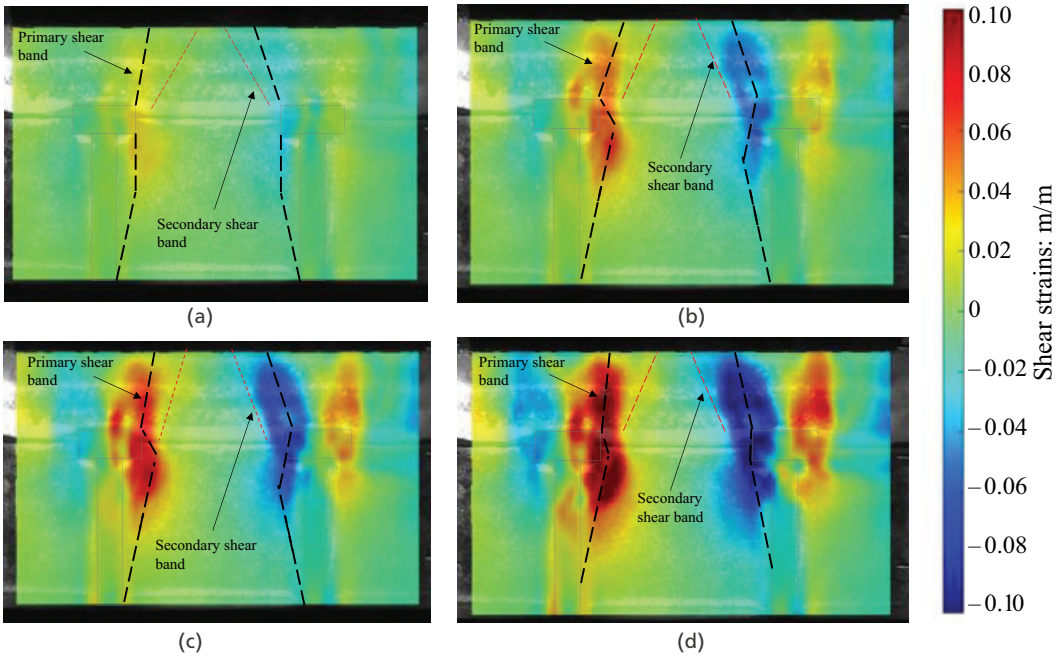

Figure 17. Shear strain contour plots for applied surcharges of (a) 15 kPa; (b) 20 kPa; (c) 25 kPa; and (d) 30 kPa

the border of the pile cap. This provides evidence that the soft foundation mobilised some shear stresses even in the presence of the arching effect, continuing the friction mobilisation observed in the granular layer. Note that the shear deformation increases with surcharge increases even inside of the clay layer. In this case, the arching effect was developed but seems not to be 100% efficient as the clay layer clearly mobilises greater stresses as surcharge increases.

The distribution of vertical strains within the physical model is depicted in Figure 18, revealing four distinct regions of vertical strain concentration. The areas of expansion (tensile) are demarcated by the black dashed lines, while the regions of compression are encircled by white dashed lines. Identifying these regions is crucial for determining the locations of maximum vertical stresses within the system, which is of importance for design analyses, as emphasised by Khatami *et al*. (2021). In general, the problem is divided in different regions of compression and vertical tensile strains. High compression regions are observed at the top of the granular layer, particularly above the outcropping of the pile caps (referred to as the stationary mass), as well as within the foundation soil mass located between the piles. Vertical tensile strains, or dilation strains, are concentrated near the top of the system, between the high compression regions over the caps. Tensile strains also develop within the granular base, forming a triangular distribution, and are present in the foundation soil between the piles and along the lateral walls of the testing box. In the granular base, a region characterised by low to medium compressive strains, located just below an area of low tensile strains, forms an arch of compression. An interesting finding in Figure 18 is the concentration of compressive strains above the caps and the presence of very low to zero strains just beneath the yielding mass between the piles, suggesting the formation of an arching effect within the granular base layer. Essentially, as the soil above the caps is compressed, the yielding mass undergoes lateral compression, leading to the development of vertical tensile strains that enhance shear mobilisation within the granular base. This behaviour is typical of soil arching mechanisms, as described by Khatami *et al*. (2021). These mechanisms create a compression zone in the form of a triangle at the base of the granular layer, corresponding to the vertical stresses transferred to the pile caps. Note that this phenomenon becomes more pronounced with increasing applied surcharge, as seen when comparing Figures 18(a) and 18(d), indicating that soil arching depends on the relative displacements between the stationery and yielding masses.

The horizontal strain distribution throughout the model is depicted in Figure 19. Negative values correspond to horizontal compressive

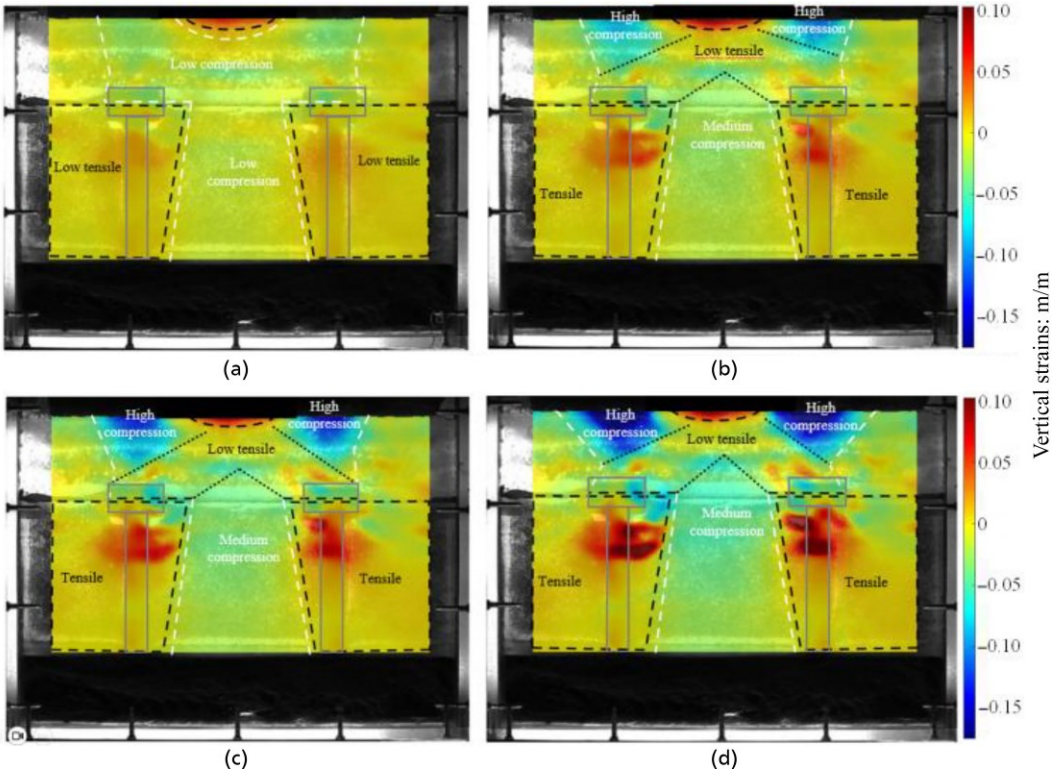

Figure 18. Vertical strain distributions under applied surcharges of (a) 15 kPa; (b) 20 kPa; (c) 25 kPa; and (d) 30 kPa

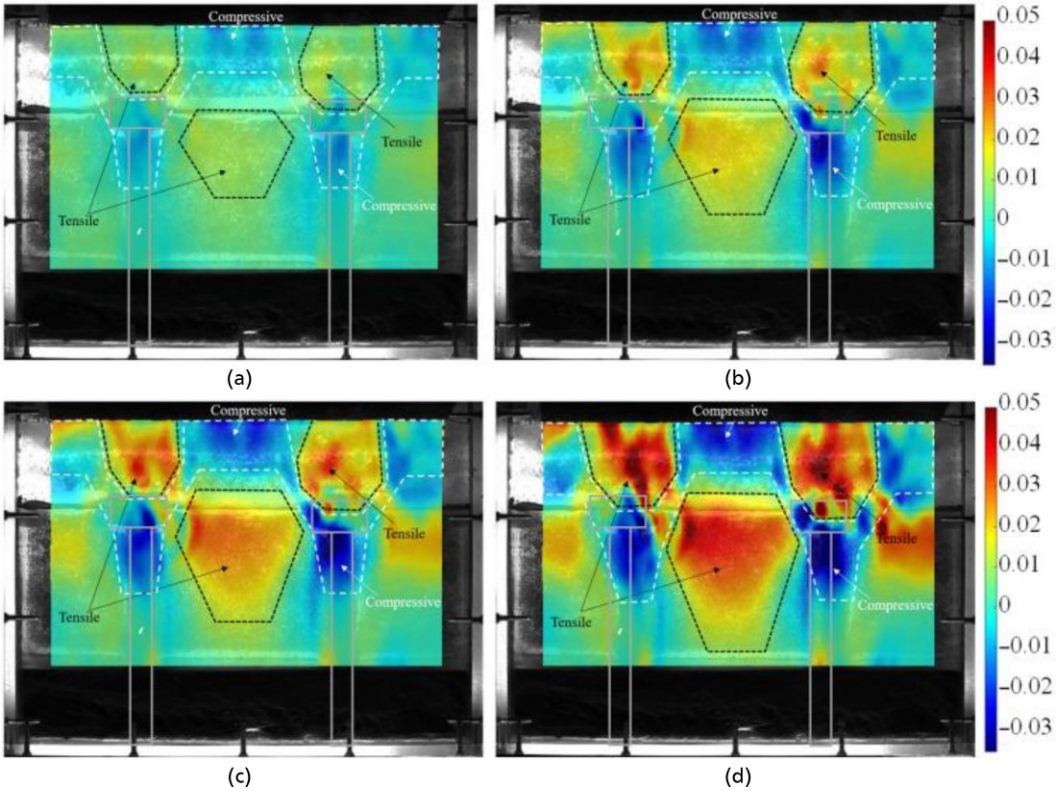

Figure 19. Horizontal strain distributions under applied surcharges of (a) 15 kPa; (b) 20 kPa; (c) 25 kPa; and (d) 30 kPa

strains, whereas positive values indicate tensile strains. Higher horizontal tensile strains were observed to occur over the pile cap and at the top of the soft soil layer. From the border of the cap, an inclined expansion line indicated the effect of the dilation of the granular material under shearing. Higher horizontal compression was observed at the centre and the top of the granular layer as well as inside the soft layer below the pile caps. A zero-stress zone is observed between the compressive zone at the top of the granular layer and the soft clay layer indicating the arching mechanism. Right below this zone, there is a tensile stress zone acting on the soft soil mass between the piles. The arching effect inside the granular layers seems to transfer horizontal compressive stresses to the piles, resulting in lateral deflections. As piles deflected horizontally, the clay layer demonstrated a shallow tensile region between piles. As vertical strains (and, as consequence, vertical stresses) are very low at this portion (Figure 18), the tensile deformation may be attributed to the fact that the clay is adhered to piles following the deflection. As the clay soil compresses along the upper length of the pile, the portion at the mid-distance between piles tends to expand under low vertical stress.

To examine the load transfer between the granular layer, the piles, and the clay layer, the stiffness of both materials (i.e. the clay and granular layers) were determined through triaxial tests. Using laponite stiffness allows us to determine the levels of vertical stress mobilised by the clay foundation layers based on the vertical strain distributions captured using the DIC analysis, as depicted in Figure 20. As illustrated in Figure 8, the values of stiffness at 4% strain were calculated, resulting in 250 kPa for the clay and 4375 kPa for the granular material, respectively, assuming lower levels confining stresses. However, the levels of confining stress acting in the laponite layer considering the arching effect are even lower (around 5 kPa). Therefore, the laponite stiffness of 40 kPa was considered, which is lower than that obtained from triaxial tests but higher than that obtained using BPT. Based on the vertical strains measured through digital correlation analysis, stresses were calculated at the centre of the clay layer and the soil above the pile caps. Two methodologies were employed to calculate the vertical stresses exerted on the pile caps. The first approach involved determining the applied load (plate load) across the entire model and assessing the stresses transferred to the top of the clay layer based on its stiffness. The disparity between these values represents the stress mobilised by the piles. The second approach focused on evaluating the vertical stresses transmitted to the foam layer situated at the model's base. Figure 10 characterises the stress–strain behaviour of the foam, facilitating the determination of vertical

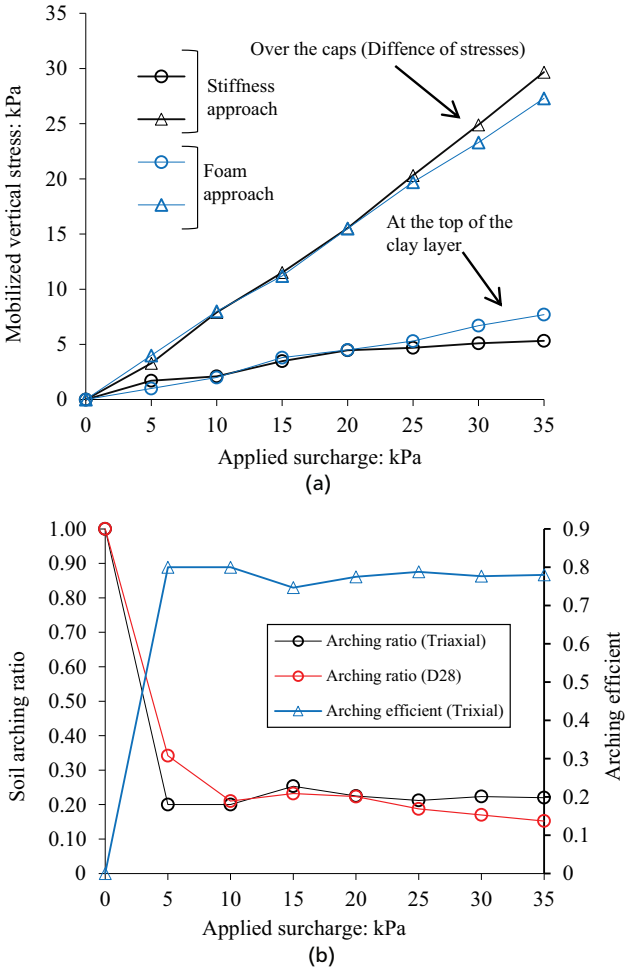

Figure 20. Analyses of stress transfer in the pile-supported embankment model tested: (a) vertical stress transferred to top of the clay layer and to the piles for each stage of surcharge and (b) soil arching ratio and arching efficiency plotted against strains at the top of the clay layer

stresses acting on the foam during tests. Subsequently, assuming negligible adhesion between the pile shaft and the clay, the vertical stress acting at the top and centre of the clay foundation layer was considered equivalent to the vertical stress measured over the foam layer. By employing both approaches, we identified stress mobilisation between the piles and the soft clay, contributing to the assessment of arching development in the pile-supported embankment model.

Figure 20(a) illustrates the average vertical stresses transmitted from the embankment to the top of the clay layer, based on the principles applied in load transfer analyses. It is noteworthy that both approaches yielded very similar results, confirming the identified stress transfer mechanisms in this investigation and validating the simplicity of using the foam layer as a reference to obtain vertical stress. Overall, it appears that the adhesion between the piles and the clay does not significantly mobilise stress levels, except for higher levels of applied surcharge (25–35 kPa), where slight variations between the approaches were observed (Figure 20(a)). The results indicate that granular layer arching develops after a surcharge of 5 kPa when relative displacements between active and stationary masses are introduced. Generally, the arching effect leads to a stress transfer of 20% to the clay foundation layer and 80% to the piles. This results in an average arching efficiency of 0.8 for all surcharge stages applied to the models. In Figure 20(b), we provide a clearer illustration of stress transfer mechanisms by plotting the arching effect ratio against the vertical strains at the top of the clay layer. The arching effect ratio was calculated as the relationship between the vertical stress at the top of the clay foundation and the applied surcharge at the loading plate, a methodology previously employed in the study by McNulty (1965). An arching effect ratio of 1:0 indicates that the applied surcharge was predominantly mobilised by the clay foundation, while lower values mean more pronounced soil arching. Figure 20(b) demonstrates that the arching effects is constant, evidencing the efficiency of arching effect in the model. An intriguing observation is that soil arching was effective even when the centre-to-centre spacing between piles was four times the pile cap width, a configuration typically regarded as excessive for developing soil arching, according to literature. This may be attributed to the relatively large average grain size of the granular material, which contributes to more substantial frictional effects and expansion.

6. Summary and conclusions

A layered transparent system was developed to conduct a comprehensive investigation of the mechanisms involved in pile-supported embankments over soft soils. This innovative technique not only provided observational results on the behaviour of small-scale physical models but also facilitated the quantification of vertical, horizontal, and shear strains developed within the embankment body and soft foundation.

One challenge encountered in this investigation was the development of a transparent sand embankment over a transparent soft clay, which was overcome by using fused quartz sand particles with a matching pore liquid as an embankment base layer and hydrated Laponite RD as a soft foundation soil. No chemical interaction occurred between materials used in this study, making this a valuable technology for the suggested application. A technique involving seeding particles was used in the model to capture the distribution of displacements and strains throughout the 2D section. The methodology presented herein is currently one of the few that facilitates the identification of arching mechanisms considering the presence of soft foundation soil, as most studies use

the trapdoor test apparatus. Based on the developments presented in this paper, the following conclusions were drawn:

- The shear band that developed within granular load transfer layers was observed to have a trapezoidal to square shape that was unchanged by applied loading. The shear bands that developed inside the granular embankment material extended to the soft soil towards the pile shaft.
- The transparency of the granular simulant facilitated confirmation of the development of an arch of stress transferring. The soil arching transferred 80% of the applied load to the piles, while 20% was mobilised by the soft foundation soil. The soil arching efficiency was not affected by the levels of applied surcharge applied over the model.
- The arching effect in the granular embankment base fill occurred even setting the centre-to-centre piles spacing of four times the cap dimension, larger than the recommendation of 2.5 times of spacing. The developed soil arching may be attributed to the large mobilisation of friction and dilation angles of the coarse embankment material with relative shearing within strain localisations.
- Unlike the results reported by many studies using trapdoor tests, the stationary mass over the pile caps generated horizontal stresses against the yielding mass developed by compression that can enhance the arching effect in the embankment granular layer.
- Although the arching effect was observed to occur in the physical model, transference of vertical and horizontal stresses to the soft foundation soil was established. Development of lateral stresses on the pile shaft were also observed because of the 20% surcharge transferred to the soil foundation.
- The mechanism of stress transference captured by the transparent model demonstrated the generation of very limited tensile and compressive zones in the vertical and horizontal directions. This information provides evidence that basal reinforcements should be applied to elevations corresponding to the first third of the granular layer to provide the membrane effect.

Data availability

The data that support the findings of this study are available from the corresponding author upon reasonable request. Due to the nature of the research, some data may not be made publicly available to protect privacy or proprietary information. The authors confirm that all relevant data are included in the paper or its supplementary materials.

Acknowledgements

The authors thank the Laboratory of Geotechnics and Geosynthetics of the Federal University of Sao Carlos. The authors also thank the Vitreous Materials Laboratory of the Federal University of Sao Carlos. Special thanks to the company Huesker Brazil for all the support in this research.

REFERENCES

ASTM (2004) ASTM D3080-04 Standard test method for direct shear test of soils under consolidated drained conditions.
ASTM (2014) ASTM D854-14 Standard test methods for specific gravity of soil solids by water pycnometer.
ASTM (2016a) ASTM D4253-16 Standard test methods for maximum index density and unit weight of soils using a vibratory table.
ASTM (2016b) ASTM D4254-16 Standard test methods for minimum index density and unit weight of soils and calculation of relative density.
ASTM (2017a) ASTM D2487-17 Standard practice for classification of soils for engineering purposes (Unified Soil Classification System).
ASTM (2017b) ASTM D2488-17 Standard practice for description and identification of soils (Visual-manual procedures).
ASTM (2018) ASTM D4318 Standard test methods for liquid limit, plastic limit and plasticity index of soils.
ASTM (2020) ASTM D7181-20 Standard test method for consolidated drained triaxial compression test for soils.
ASTM (2023) ASTM D2850-23 Standard test method for unconsolidated-undrained triaxial compression test on cohesive soils.
Ads A, Iskander M and Bless S (2020a) Shear strength of a synthetic transparent soft clay using a miniature ball penetrometer test. *Geotechnical Testing Journal* **43(5)**: 1248–1268, 10.1520/GTJ20190020.
Ads A, Iskander M and Bless S (2020b) Soil–projectile interaction during penetration of a transparent clay simulant. *Acta Geotechnica* **15(4)**: 815–826, 10.1007/s11440-020-00921-z.
Almikati A, Pierozan RC, Sadek S and Zornberg JG (2023) Geotechnical characterization of Laponite as transparent clay surrogate. *Geotechnical Testing Journal* **46(3)**: 535–558.
Beemer RD and Aubeny CP (2012) Digital image processing of drag embedment anchors in translucent silicate gel, *Proceedings of GeoManitoba*
Beemer RD, Shaughnessy E, Ewert KR *et al.* (2016) The use of sodium pyrophosphate to improve a translucent clay simulant. *Journal of Chemical Information and Modeling* **53(9)**: 1689–1699, 10.1017/CBO9781107415324.004.
Blaber J, Adair B and Antoniou A (2015) Ncorr: open-source 2D digital image correlation Matlab software. *Experimental Mechanics* **55(6)**: 1105–1122, 10.1007/s11340-015-0009-1.
Cao Z, Liu J and Liu H (2011) Transparent fused silica to model natural sand, *Pan-Am CGS Geotechnical Conference*.
Carvalho T, Suescun-Florez E, Omidvar M and Iskander M (2015) A nonviscous water-based pore fluid for modeling with transparent soils. *Geotechnical Testing Journal* **38(5)**: 805–811, 10.1520/GTJ20140278.
Chen JF, Gu Z-A, Rajesh S and Yu S-B (2021) Pullout behavior of triaxial geogrid embedded in a transparent soil. *International Journal of Geomechanics* **21(3)**: 04021003, 10.1061/(asce)gm.1943-5622.0001936.
Chen JF, Guo XP, Xue JF and Guo PH (2019a) Failure analysis of reinforced foundation using transparent soils. In *Environmental Science and Engineering*, vol. 1, pp. 649–657, 10.1007/978-981-13-2224-2_80.
Chen JF, Guo XP, Xue JF and Guo PH (2019b) Load behaviour of model strip footings on reinforced transparent soils. *Geosynthetics International* **26(3)**: 251–260, 10.1680/jgein.19.00003.
Chen JF, Guo X, Sun R *et al.* (2021) Physical and numerical modelling of strip footing on geogrid reinforced transparent sand. *Geotextiles and Geomembranes* **49(2)**: 399–412, 10.1016/j.geotexmem.2020.10.011.

Ezzein FM and Bathurst RJ (2011) A transparent sand for geotechnical laboratory modeling. *Geotechnical Testing Journal* **34(6)**: 590–601, 10.1520/GTJ103808.

Ezzein FM and Bathurst RJ (2014) A new approach to evaluate soil-geosynthetic interaction using a novel pullout test. *Geotextiles and Geomembranes* **42(3)**: 246–255, 10.1016/j.geotexmem.2014.04.003.

Ferreira JAZ and Zornberg JG (2015) A transparent pullout testing device for 3D evaluation of soil-geogrid interaction. *Geotechnical Testing Journal* **38(5)**: 686–707, 10.1520/GTJ20140198.

Gill DR and Lehane BM (2001) An optical technique for investigating soil displacement patterns. *Geotechnical Testing Journal* **24(3)**: 324–329.

Guzman EMD and Alfaro M (2016) Modelling a highway embankment on peat foundations using transparent soil. *Procedia Engineering* **143**: 363–370, 10.1016/j.proeng.2016.06.046.

Ganiyu AA, Rashid ASA and Osman MH (2016) Utilisation of transparent synthetic soil surrogates in geotechnical physical models: a review. *Journal of Rock Mechanics and Geotechnical Engineering* **8(4)**: 568–576, 10.1016/j.jrmge.2015.11.009.

Guzman IL, Iskander M, Suescun-Florez E and Omidvar M (2014) A transparent aqueous-saturated sand surrogate for use in physical modeling. *Acta Geotechnica* **9(2)**: 187–206.

Iai S (1989) Similitude for shaking table tests on soil-structure-fluid model in 1g gravitational field. *Soils and Foundations* **29(1)**: 105–118.

Iskander M and Liu J (2010) Spatial deformation measurement using transparent soil. *Geotechnical Testing Journal* **33(4)**: 314–321, 10.1520/GTJ102745.

Iskander MG, Liu J and Sadek S (2002) Transparent amorphous silica to model clay. *Journal of Geotechnical and Geoenvironmental Engineering* **128(3)**: 262–273, 10.1061/(ASCE)1090-0241(2002)128:3(262).

Khatami H, Deng A and Jaksa M (2021) Mapping soil arching-induced shear and volumetric strains in dense sands. *Transportation Geotechnics* **28**: 100547.

Kong G, Zhou Y, Yang Q *et al.* (2020) Geotechnical properties of a new transparent clay. *International Journal of Geomechanics* **20(12)**: 06020032, 10.1061/(asce)gm.1943-5622.0001880.

Liu J and Iskander MG (2010) Modelling capacity of transparent soil. *Canadian Geotechnical Journal* **47(4)**: 451–460, 10.1139/T09-116.

Liu C, Tang X, Wei H *et al.* (2020) Model tests of jacked-pile penetration into sand using transparent soil and incremental particle image velocimetry. *KSCE Journal of Civil Engineering* **24(4)**: 1128–1145, 10.1007/s12205-020-1643-4.

Liu J, Iskander MG and Sadek S (2003) Consolidation and permeability of transparent amorphous silica. *Geotechnical Testing Journal* **26(4)**: 390–401, 10.1520/gtj11257j.

Ma S, Duan Z, Huang Z *et al.* (2022) Study on the stability of shield tunnel face in clay and clay-gravel stratum through large-scale physical model tests with transparent soil. *Tunnelling and Underground Space Technology* **119**: 104199, 10.1016/j.tust.2021.104199.

McNulty JW (1965) An experimental study of arching in sand. *Technical Report No. 1-674*. Army Engineer Waterways Experiment Station, Vicksburg, MS, USA.

Morsy AM, Zornberg JG, Han J and Leshchinsky D (2019) A new generation of soil-geosynthetic interaction experimentation. *Geotextiles and Geomembranes* **47(4)**: 459–476, 10.1016/j.geotexmem.2019.04.001.

Ni Q, Hird CC and Guymer I (2010) Physical modelling of pile penetration in clay using transparent soil and particle image velocimetry. *Géotechnique* **60(2)**: 121–132, 10.1680/geot.8.P.052.

Peng X and Zornberg JG (2019) Evaluation of soil-geogrid interaction using transparent soil with laser illumination. *Geosynthetics International* **26(2)**: 206–221, 10.1680/jgein.19.00004.

Pierozan RC, Almikati A, Silva Araujo GL and Zornberg JG (2022) Optical and physical properties of Laponite for use as clay surrogate in geotechnical models. *Geotechnical Testing Journal* **45(1)**: 79–100, 10.1520/GTJ20210100.

Rui R, Han J, Van Eekelen SJM and Wan Y (2019) Experimental investigation of soil-arching development in unreinforced and geosynthetic-reinforced pile-supported embankments. *Journal of Geotechnical and Geoenvironmental Engineering* **145(1)**, 10.1061/(asce)gt.1943-5606.0002000.

Rui R, Van Tol AF, Xia YY *et al.* (2016) Investigation of soil-arching development in dense sand by 2D model tests. *Geotechnical Testing Journal* **39(3)**: 20150130–20150430, 10.1520/GTJ20150130.

Rui R, Zhai YX, Han J *et al.* (2020) Deformations in trapdoor tests and piled embankments. *Geosynthetics International* **27(2)**: 219–235, 10.1680/jgein.19.00014.

Skinner AE (1969) A note on the influence of interparticulate friction on the shearing strength of a random assembly of spherical particles. *Géotechnique* **19(1)**: 150–157.

Sadek S, Iskander MG and Liu J (2002a) Geotechnical properties of transparent silica. *Canadian Geotechnical Journal* **39(1)**: 111–124, 10.1139/t01-075.

Sadek S, Liu J and Iskander MG (2002b) Optical measurement of deformation using transparent silica gel to model sand. *International Journal of Physical Modelling in Geotechnics* **2(4)**: 13–26, 10.1680/ijpmg.2002.2.4.13.

Sadek S, Iskander MG and Liu J (2003) Accuracy of digital image correlation for measuring deformations in transparent media. *Journal of Computing in Civil Engineering* **17(2)**: 88–96, 10.1061/(ASCE)0887-3801(2003)17:2(88).

Viswanadham BVS and König D (2004) Studies on scaling and instrumentation of a geogrid. *Geotextiles and Geomembranes* **22(5)**: 307–328, 10.1016/S0266-1144(03)00045-1.

Wallace JF and Rutherford CJ (2015) Geotechnical properties of LAPONITE RD®. *Geotechnical Testing Journal* **38(5)**: 574–587, 10.1520/GTJ20140211.

Wallace JF, Rutherford CJ and Zheng J (2018) Visualizing failure surfaces in soft clay due to suction caisson loading. *Geotechnical Special Publication*: 172–180, 10.1061/9780784481578.018.

Wang J, Long Y, Gao F *et al.* (2022) Transparent soil test evaluation of vertical–horizontal mixed curtain during dewatering. *Acta Geotechnica* **17(8)**: 3293–3313, 10.1007/s11440-021-01436-x.

Wei L, Xu Q, Wang S *et al.* (2019) Development of transparent cemented soil for geotechnical laboratory modelling. *Engineering Geology* **262**: 105354–105358, 10.1016/j.enggeo.2019.105354.

Xu G, Iskander M, Ads A and Jing H (2021) Visualizing the effect of excavation rate on rock deformation and fracturing of tunnels using a transparent soft rock surrogate. *Acta Geotechnica* **17(5)**: 1949–1969, 10.1007/s11440-021-01333-3.

Yang Q, Shao J, Xu Z and Miao Y (2022) Experimental investigation of the impact of necking position on pile capacity assisted with transparent soil technology. *Advances in Civil Engineering* **2022(1)**, 10.1155/2022/9965974.

Yang X, Jin G, Huang M and Tang K (2020) Material preparation and mechanical properties of transparent soil and soft rock for model tests. *Arabian Journal of Geosciences* **13(10)**, 10.1007/s12517-020-05325-7.

Yuan B, Sun M, Xiong L *et al.* (2020) Investigation of 3D deformation of transparent soil around a laterally loaded pile based on a hydraulic gradient model test. *Journal of Building Engineering* **28**: 101024, 10.1016/j.jobe.2019.101024.

Zhao H and Ge L (2007) Dynamic properties of transparent soil. *Journal of Performance of Constructed Facilities*: 1–9, 10.1061/40904(223)14.

Zhang W, Zhong H, Xiang Y *et al.* (2020) Visualization and digitization of model tunnel deformation via transparent soil testing technique. *Underground Space* **7(4)**: 564–576, 10.1016/j.undsp.2020.05.004.

Zhang Z, Tao F-J, Han J *et al.* (2021) Arching development in transparent soil during multiple trapdoor movement and surface footing loading. *International Journal of Geomechanics* **21(3)**: 04020262, 10.1061/(asce)gm.1943-5622.0001908.